Microstructure and mechanical properties of electron beam weld joints of a $Zr_{41}Ti_{14}Cu_{12}Ni_{10}Be_{23}$ bulk metallic glass with Zr

R. Bhowmick
Department of Materials Engineering, Indian Institute of Science, Bangalore 560012, India

S. Bysakh
Defense Metallurgical Research Laboratory, Hyderabad 500058, India

Y. Kawamura and M. Yamasaki
Department of Materials Science and Engineering, Shock Wave and Condensed Matter Research Center, Kumamoto University, Kumamoto 860-8555, Japan

U. Ramamurty and K. Chattopadhyay[a)]
Department of Materials Engineering, Indian Institute of Science, Bangalore 560012, India

(Received 14 September 2006; accepted 10 October 2006)

The electron beam welding technique was used to join $Zr_{41}Ti_{14}Cu_{12}Ni_{10}Be_{23}$ bulk metallic glass (BMG) to crystalline pure Zr. Compositional, microstructural, and mechanical property variations across the welded interface were evaluated. It is shown that a crystalline layer develops close to the welding interface. Transmission electron microscopy of this layer indicates the crystalline phase to be tetragonal with lattice parameters close to that reported for Zr_2Ni. However, the composition of this phase is different as it contains other alloying additions. The interface layer close to the bulk metallic glass side contains nanocrystalline Zr_2Cu phase embedded in the glassy matrix. Nanoindentation experiments indicate that the hardness of the crystalline layer, although less than the bulk metallic glass, is more than the Zr itself. Commensurately, tensile tests indicate that the failure of the welded samples occurs at the Zr side rather than at the weld joint.

I. INTRODUCTION

Bulk metallic glasses (BMGs) are candidate materials in many structural applications because of their attractive mechanical properties such as high strength and stiffness. Further, they possess good workability and formability above the glass transition temperature, T_g.[1] However, components made of BMGs must be joined with other metallic structural components in many structural application scenarios. Welding is by far the most popular joining technique in industrial practice. Kawamura and coworkers[2–4] have demonstrated the success of several welding processes, namely, friction, spark, pulse current, and electron beam welding (EBW) in joining BMGs with other crystalline metallic materials. Other techniques such as the use of Ni/Al multilayer foils capable of producing a self-propagating exothermic reaction have also been used for welding of amorphous alloys with other metals.[5]

One of the BMGs that has a good potential for structural engineering applications is $Zr_{41}Ti_{14}Cu_{12}Ni_{10}Be_{23}$ (Vit1).[1] This BMG exhibits an excellent glass forming ability (GFA) and can be processed for various sizes and shapes by simple casting processes at low cooling rates. However, available sample thickness and size continue to be limiting parameters for structural applications. Therefore, joining with other structural elements is an alternate possibility for overcoming these limitations. The scientific issues associated with welding of the metallic glass with crystalline counterparts include the issue of interdiffusion and the crystallization associated with the thermal cycling that welding process imposes. Consequent variation of the mechanical properties across the weld zone is also of concern because it has been shown recently that partial-crystallization or structural relaxation can induce severe embitterment to BMGs.[6–9] Keeping these in view, detailed characterization of a sound weld that was produced by EBW technique was undertaken in this study. In this article, we report the microstructure and mechanical properties across the welded interface of Vit1 with Zr base metal.

[a)]Address all correspondence to this author.
e-mail: kamanio@materials.iisc.ernet.in
DOI: 10.1557/JMR.2007.0046

II. MATERIALS AND EXPERIMENTS

The Vit1 BMG plates with 3.5 mm thickness, 10 mm width, and 40 mm length were welded to polycrystalline pure Zr coupon in butt geometry. The welding was carried out in a vacuum of 5×10^{-2} Pa using an electron beam welder of maximum power 9 kW. Figure 1 is a schematic illustration of the electron beam welding process. An accelerating voltage of 60 kV and a beam current of 20 mA with equal working and focus distances of 30 mm and a beam scanning velocity of 33 mm/s were used. These optimum conditions for welding were arrived at, after several iterations.[2]

The quality of the welds produced was assessed, in addition to visual and optical microscopy inspections, by subjecting the welded beams to bending. The welding process was considered optimum if the weld joints can withstand a 90° bending. Preliminary assessment shows that it is possible to achieve 90° bending without cracking the weld joint, indicating the possibility of getting high quality weld joints between Zr and Vit1 BMG by employing the electron beam welding technique.[2]

A JEOL (Tokyo, Japan) JSM-840A scanning electron microscope was utilized to examine the microstructure of the welded samples. X-ray diffractometry (XRD) was performed across the weld interface by using collimated Cu K_α radiation in a JEOL JDX-8030 diffractometer, with a beam of 0.5 mm width. The polished cross section was investigated by an electron probe microanalyzer (EPMA, Cameca SX 100 series, Gennevilliers, France) to examine the extent of alloying that took place during welding. Transmission electron microscopy (TEM) of the weld interface was conducted using JEOL 2000FXII and TECNAI (FEI Company, Hillsboro, OR) 200 KV microscopes. The specimen for the TEM investigation was prepared using a GATAN (Pleasanton, CA) ion mill.

Given that only a small volume of material is available for mechanical characterization, indentation technique was used to characterize the weld joints. Recently, it has been demonstrated that this technique can be successfully used to evaluate the mechanical properties as well as understand the deformation behavior of BMGs.[10–13] Further, the nanoindentation technique provides the necessary spatial resolution to evaluate properties as a function of distance away from the weld interface. Elastic modulus, E, and hardness, H, variation across the welded interface was evaluated by using a nanoindenter (Hysitron Triboindenter, Minneapolis, MN) employing a diamond Berkovich tip. The load, P, versus depth of penetration, h, curves obtained were corrected for any drift through auto-calibration before each indentation experiment was performed. A distance of ~10 μm between the indents was maintained to minimize any deformation field interaction. A maximum load of 5 mN with a loading/unloading rate of 0.5 mN/s was applied with a 5 s hold time at peak load. Measurements far away from the welded region were also conducted for comparison purposes. The elastic modulus values were deconvoluted from that of the relative modulus values by using the formula

$$\frac{1}{E_r} = \frac{1-\gamma_s^2}{E_s^2} + \frac{1-\gamma_i^2}{E_i^2} \quad , \tag{1}$$

where E_r is the reduced modulus (extracted from the slope of the unloading curve using the Oliver-Pharr method[14]), E_s and E_i are the elastic moduli of the specimen and the indenter, respectively, with γ_s and γ_i being the respective Poisson's ratios. For computing the E_s from the measured E_r, $E_i = 1141$ GPa, $\gamma_i = 0.07$, and $\gamma_s = 0.35$ were used.

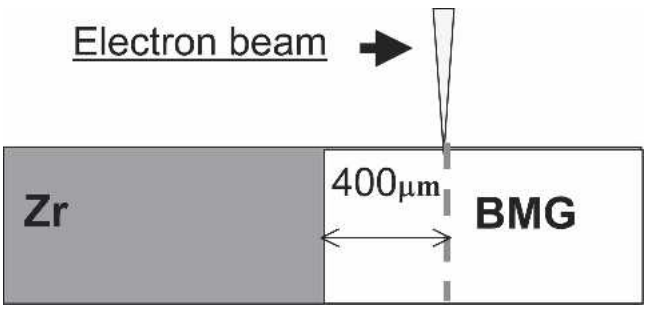

FIG. 1. Schematic of the electron beam welding configuration used in the present work.

III. RESULTS

A. Microstructural analysis

Low magnification scanning electron micrograph of the transverse section of the weld joint is shown in Fig. 2(a). A bead, characterized by bulging, is present on the BMG side. Bead formed both on the upper and lower sides of the plates, suggesting that for a current of 20 mA the electron beam penetrated through the 3.5 mm thick plate. A distinct contrast between the metallic glass and crystalline Zr was seen even in the unetched condition. The size of the weldment is about 1.5 mm. (The term weldment is used here to refer to the region showing a different contrast to that of the BMG and Zr.) No visible defects like pores or cracks in both the bead and heat affected zone (HAZ) could be detected near the weldment.

XRD scans of the Zr-glass interface [marked by arrows in Fig. 2(a)] fail to reveal any other phase besides α-Zr and glass, as shown in Fig. 2(b). There seems to be a smooth transition from the broad diffuse maxima on the metallic glass side to the diffraction peaks of Zr phase. Diffraction patterns, obtained using a microfocus beam of 50 μm diameter, also did not reveal existence of any additional phase.

A low magnification SEM micrograph of the transverse section of the polished and etched welded sample

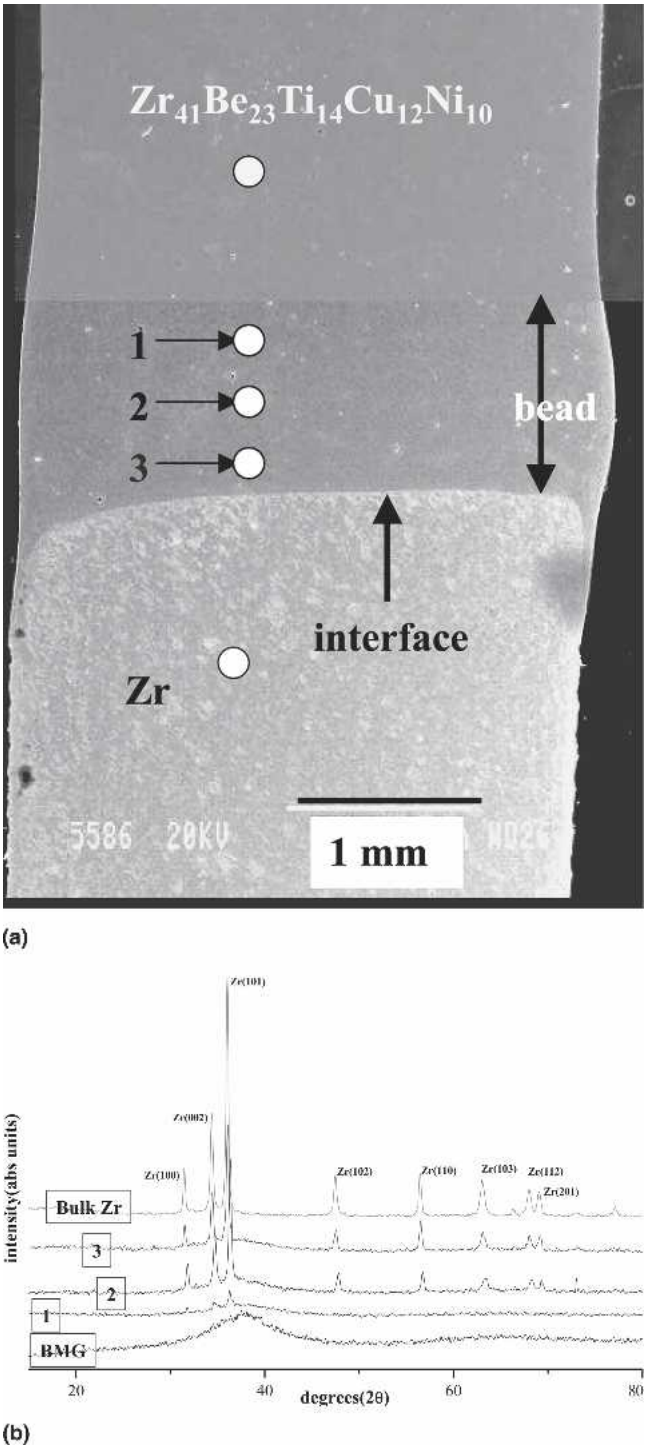

FIG. 2. (a) Cross-sectional image of crystal Zr electron beam welded to $Zr_{41}Cu_{12}Ti_{14}Ni_{10}Be_{23}$ BMG. (b) XRD scans obtained across the welded Zr-glass interface at different spots marked in (a).

of glass with the Zr is shown in the inset of Fig. 3(a). The micrograph illustrates the presence of a sharp interface toward the Zr side while the weldment extends into the BMG side. The alloyed region is ~60 μm wide, of a total length of ~1 mm of the weldment. The rest of the weldment is the heat affected zone. On deep etching, microstructure very close to the interface was revealed, which is shown in Fig. 3(a). This welded interface image, obtained in the backscattered electron mode, reveals the growth of a dendritic phase from the Zr interface into the glass. Further, it suggests an oriented growth of dendrites with respect to the interface. However, the dendrites do not appear to grow normal to the interface at the initial stage. This observation implies that the initial growth is influenced by the easy crystallographic direction for the growth of the phase from the Zr/glass interface. The initial dendrites are coarser and extend to a distance of ~8 μm with an approximate secondary arms spacing of 1 μm. A transition in the scale of dendrites to finer, with smaller secondary dendrite spacing of ~0.3 μm and with decreasing spacing with distance away from the interface, occurs beyond a distance of ~8.5 μm from the interface. This is illustrated by the white dotted line highlighting one primary dendrite revealing the features clearly. At this stage, the morphology of the secondary dendrites suggests that they align normal to the original Zr-glass interface.

In general, the change in the scale of the dendrite and their arms spacing indicates a change in the growth rate with finer spacing representing a higher growth rate. Kurz and coworkers have established that the dendrite morphology is sensitive to their growth rate.[15,16] Beyond a critical growth rate, a sudden change in the morphology can be expected with coarser dendrites getting replaced by thinner needle-like dendrite with a change in the tip radius. Thus our observation can be correlated with the continuous increase in the growth rate until the growth is inhibited by the increase in the viscosity of the liquid ahead, which can affect the atomic jump and hence diffusivity. However, in actual practice the situation is likely to be significantly more complicated. The dendritic growth in the present case takes place in the presence of a concentration gradient. Assuming that it involves primarily the jump of Zr atoms, the decreasing concentration of Zr indicates a continuous decrease of the chemical potential.

Electron probe microanalyzer (EPMA) analysis of the composition of the various alloying elements [Fig. 3(b)] indicates there is very little interdiffusion and alloying on the Zr side during welding. The base metal composition adjacent to the interface remains unaffected by the welding process. On the BMG side of the interface, a concentration gradient in all the alloying elements is seen, with a span of ~70 μm, beyond which the at.% reaches that of Vit1's composition. In particular, the changes in the Zr and Be concentration are distinct in this 70-μm-thick region, which also corresponds approximately to the thickness of the crystallized region in Fig. 3(a). A careful examination reveals that except for the

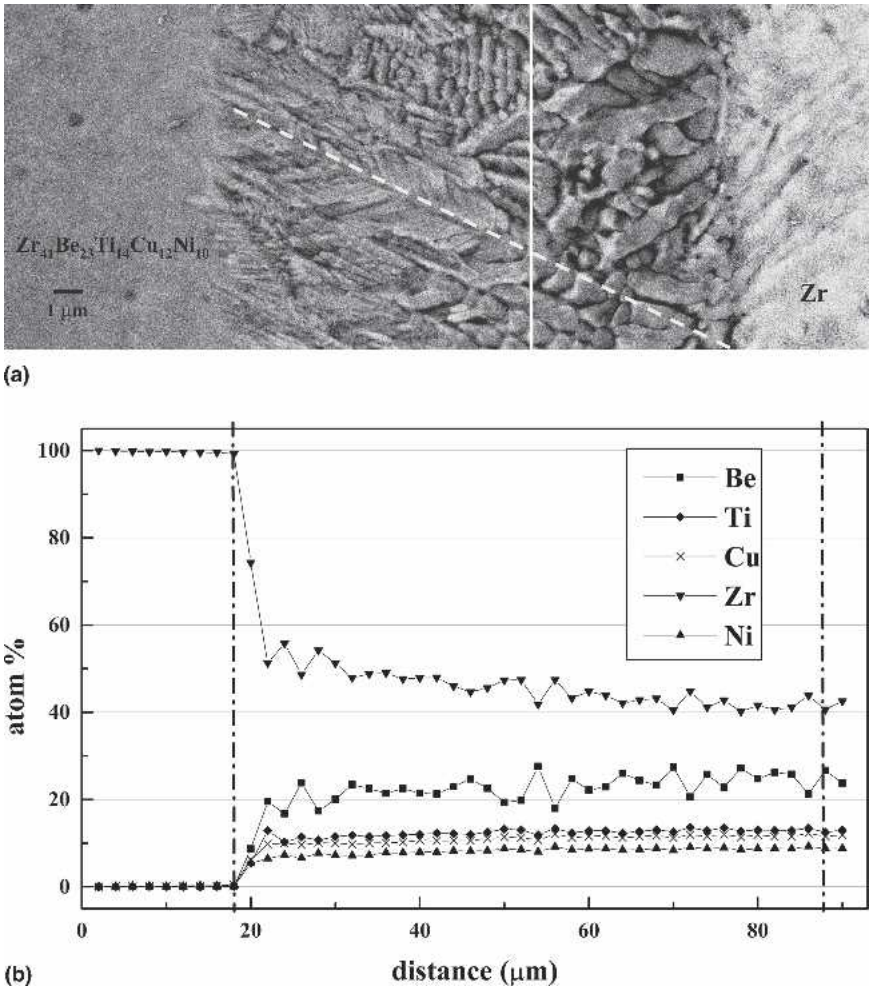

FIG. 3. (a) SEM images of the etched cross section around the Zr-glass interface. (b) EPMA composition profiles across the welded interface for Zr-glass weld.

region very close to the Zr interface (~10 μm wide) the gradient of composition is primarily that of Zr, which appears to get enriched.

To further characterize the interface regions of the weldment, detailed TEM examination of the weldment was carried out. Figure 4(a) shows a low magnification bright-field image of the interface exhibiting the morphology of the dendrites. The diffraction patterns, taken from the interdendritic space (shown in the inset), exhibit diffuse halo characteristic of the glassy phase. The dark-field image at high magnification, taken with a portion of the diffuse halo, shows speckle contrast indicating the possibility of the existence of some clusters [Fig. 4(b)]. The morphology of the dendrites can be clearly seen in Fig. 4(c). Diffraction pattern from the region marked in the image exhibits single crystal pattern [Fig. 4(d)]. Detailed examination of these dendrites reveals dislocation substructures, suggesting plastic deformation of the crystalline phase during cooling subsequent to welding.

To determine the structure of the dendritic phase, systematic tilting experiments were carried out. Figure 5 shows a typical sequence of the diffraction patterns under different tilting conditions. The patterns can be consistently indexed in terms of a tetragonal lattice with $a = 0.66$ nm and $c = 0.542$ nm. The lattice parameters are close to that reported for the Zr_2Ni phase suggesting that the observed phase is isomorphous to Zr_2Ni.[17] The microstructure suggests heterogeneous nucleation of this phase on the unmelted Zr substrate and subsequent growth into the glass. No evidence of the formation of Be containing Zr_2Be phase could be observed during the welding process.

The microstructure of the glass close to the crystalline weld zone is shown in Fig. 6. One can observe very fine crystalline particles embedded in the glassy matrix. The selected area diffraction patterns from these regions exhibit Debye Scherrer rings in addition to the diffuse ring due to the amorphous phase. The rings can be indexed in terms of the Zr_2Cu phase.

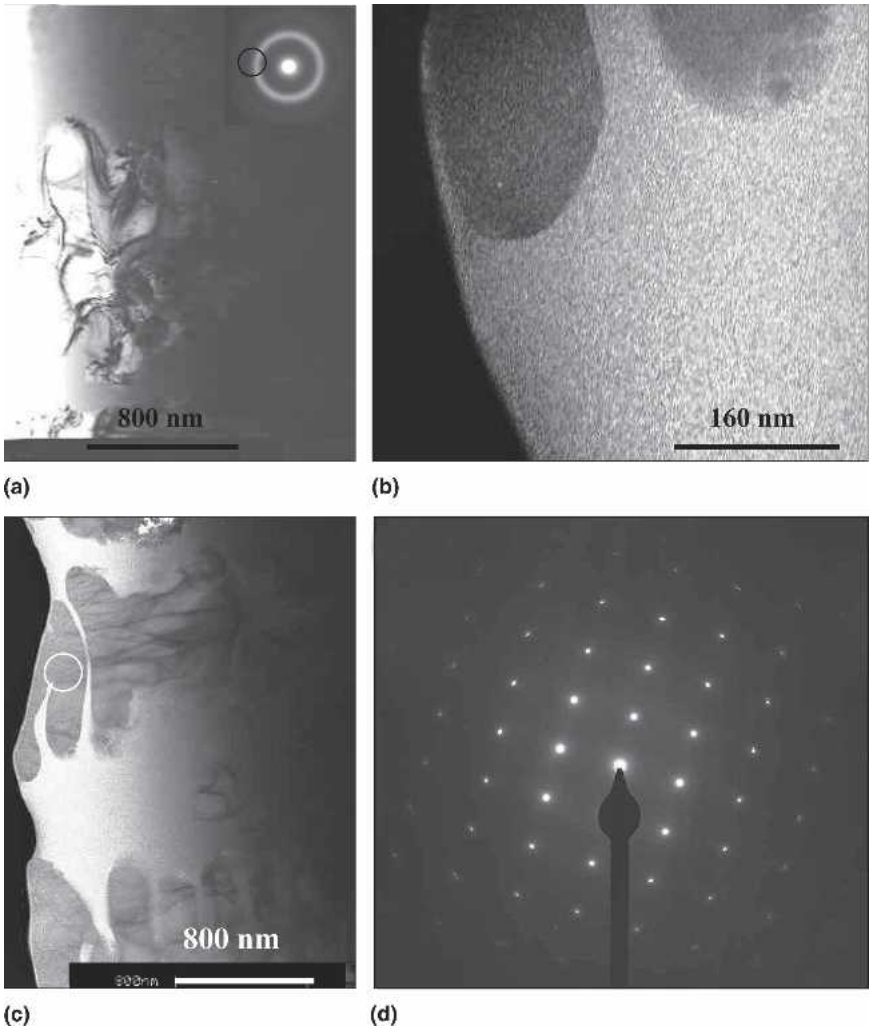

FIG. 4. TEM images of the dendritic phase observed at the weld interface. (a) Low magnification bright-field image of the dendrite and surrounding amorphous phase. (Inset shows SAD from glassy region.). (b) Dark-field image from a portion of the diffuse halo indicating speckle contrast. (c) Bright-field image showing typical morphology of the secondary arm of the dendrite. (d) Selected area diffraction (SAD) pattern from the dendrite obtained from the circled region in (c).

B. Mechanical properties

To explore the mechanical properties of the welded joint further, the welded samples were tested in tension (with the weld line perpendicular to the loading axis). In all cases, fracture of the specimen occurred within the Zr part of the weld, indicating that weld has much higher strength than the Zr itself. This also indicates the sound nature of the welded joint. Figure 7(a) shows an array of nanoindents extending from the metallic glass to the crystalline Zr side. The BSE image also shows the dendritic structure present at the interface. The change in indent size as one cross over from the Zr to the glass side is evident in the SEM images of the interface. Thus as expected the hardness values jump from a value of about 2.61 GPa on the Zr side to a high value of 7.1 GPa on the Vit1 side of the weld [Fig. 7(b)]. The change in the elastic modulus across the interface, however, exhibits a different behavior [Fig. 7(c)]. It shows a dip from a value close to 110 GPa on the Vit1 side to a low of 85 GPa or even lower in the region very close to the interface before rising back to about 90 GPa on the Zr side of the weld. The dip is observed to occur in the same area that shows dendritic growth.

IV. DISCUSSION

Results presented in the preceding section show that it is possible to get sound joints between Zr and Vit1 BMG with the aid of EBW technique, with crystallization of the amorphous alloy being restricted to a narrow region of ~70 μm while dendritic growth took place very close to the Zr interface (~10 μm). Further, results of the nanoindentation experiments show this dendritic region has only marginally lower E values whereas the hardness

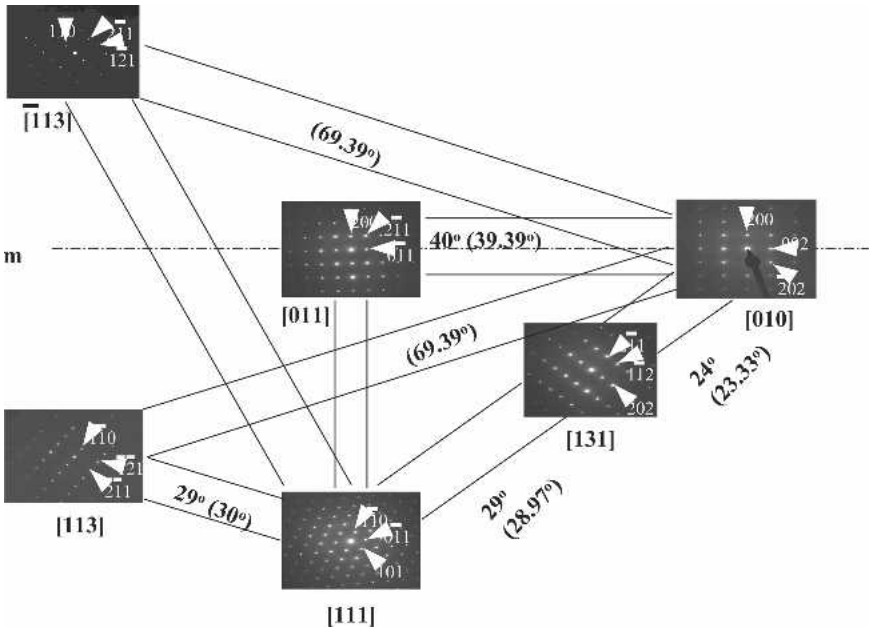

FIG. 5. SADPs taken along different zones from the fragment of a dendrite. The patterns and their angular relations can be completely rationalized in terms of a tetragonal phase that is isomorphous with the Zr_2Ni phase.

is not affected. Microstructure evaluation indicates that the glass phase is completely molten during the welding process, whereas the pure Zr does not melt. This was to be expected as the eutectic temperature of Vit1 is 1100 K, which is almost half of that of the melting point of Zr.

The melt of Vit1 during cooling is expected to vitrify as the cooling rate that it experiences during dissimilar electron beam welding (~10^2 to 10^3 K/s), is higher than the critical cooling rate required for glass formation in Vit 1 (~1 K/s). Typically the heating/cooling cycle of the welding process is over within 10 s, whereas the nose time for the TTT curve for Vitralloy 1 is 50–70 s.[18] Therefore, the observed crystallization must be explained in terms of the Zr enrichment of the metallic glass near the interface during the melting process due to the diffusion of Zr from the crystalline side into the melt. The EPMA results do indicate the enrichment of Zr near the interface and hence support this possibility.

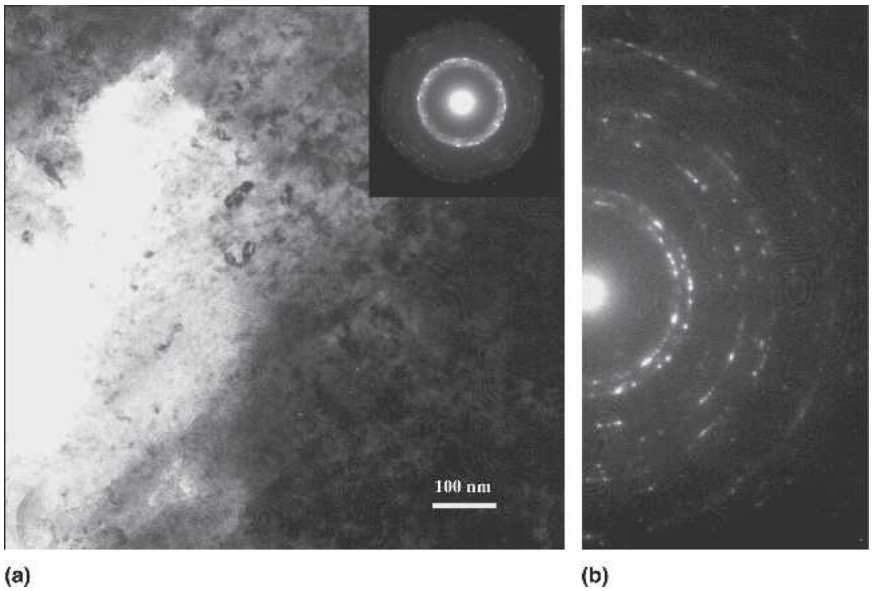

FIG. 6. Bright-field image of the BMG adjacent to the crystalline region of the weld pool. The fine crystal in the matrix yield the Debye Scherrer rings in the diffraction pattern shown in the inset. (b) A blow-up of the SAD showing the Zr_2Cu reflections.

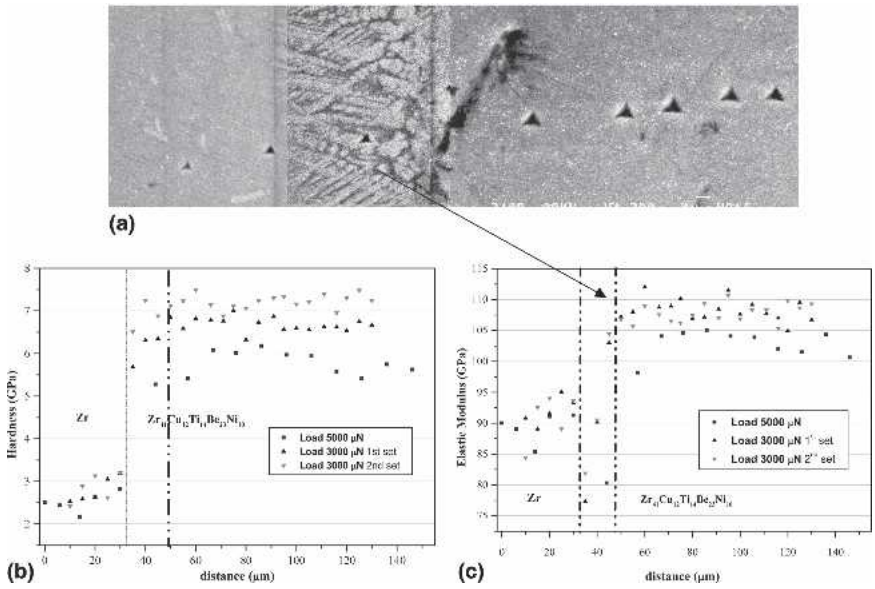

FIG. 7. (a) Backscattered SEM micrograph showing a series of nanoindents across the weld interface. (b) Hardness and (c) elastic modulus profiles across the welded interface.

Crystallization and dendrite growth process can be further understood by examining the pseudo ternary (Zr,Ti)-(NiCu)-Be diagram (Fig. 8 in Ref. 19). The Vit1 has a high GFA, having a critical cooling rate of <10 K/s. However, the alloyed region of weldment has reduced GFA (due to the dilution by Zr) and hence crystallizes while solidifying from the melt. Once crystallization sets in by heterogeneous nucleation at the Zr-side of the interface, growth of the crystals occurs toward the BMG side in a dendritic manner.

The observation of Zr_2Ni type phase as the primary dendrite in Vit1 during processing is well known and arises from local changes in composition. Thus our observation of the nucleation of a phase similar to Zr_2Ni toward the Zr side of the weld interface is not surprising. However, the chemical analysis of this phase indicates the following composition (in at.%): Zr—74.2-77.5, Cu—9.5-13.2, Ni—6.2-7.6, and Ti—3.2-5.4. Although Be detection is not possible with this technique, the structure of the phase (similar to Zr_2Ni) suggests that it may contain significant amounts of Be to compensate for the presence of higher (than stoichiometric) Zr. In the absence of any compound of Be, the excess Be must partition into the glass surrounding the dendrite. Undercooled Vit1 liquid melt has been reported to phase separate into Zr rich and Be rich phases.[19,20] This can also account for the opposite trend in composition fluctuations of Zr and Be, seen in the alloyed region of the Zr-glass weld [Fig. 3(b)]. The Zr richer regions are known to be thermally less stable than the Be rich regions with respect to crystallization[21] and hence can account further for the enhanced dendritic growth close to the welded interface, whereas further away from it the dendritic growth is arrested.

Further away from the interface, in the HAZ, the heating rather than the cooling part of the curve will have more influence, with devitrification playing a major role. Upon annealing Vit1 near the glass transition temperature and up to a temperature near 673 K, a Be containing phase forms. Annealing above 673 K produces Be_2Zr and Zr_2Cu along with other crystalline phases.[22] The TEM studies of the alloyed region of the Zr-glass weld away from the dendritic region reveal precipitation of fine Zr_2Cu in the glassy matrix. This indicates that in this region the devitrification occurs during the heating cycle yielding the fine crystallites.

Although the weld interface contains crystalline intermetallic compounds, tensile testing of the welded joints indicate that this layer is stronger than the Zr and hence does not affect the joint during mechanical loading. This implication is further supported by the nanoindentation studies.

V. CONCLUSIONS

(1) Electron beam welding can produce a sound weld to join elemental Zr with $Zr_{41}Ti_{14}Cu_{12}Ni_{10}Be_{23}$ (Vit1).

(2) A crystalline layer develops at the interface. The origin of this layer is explained in terms of diffusion of Zr in the molten BMG during heating and a consequent decrease in glass forming ability.

(3) The structure of the crystalline layer is tetragonal ($a = 0.66$ nm and $c = 0.542$ nm) and is similar to that reported for intermetallic compound Zr_2Ni. However, composition of this phase is different. No evidence of any Be rich crystalline phase could be observed.

(4) The results of the nanoindentation studies indicate the crystalline region to be harder than the Zr. The failure

during tensile testing occurs in the Zr side and not at the joint, implying a sound weld.

ACKNOWLEDGMENT

This work at the Indian Institute of Science was funded by a grant from the Defense Research and Development Organization, Ministry of Defense, Government of India.

REFERENCES

1. W.L. Johnson: Bulk glass-forming metallic alloys: Science and technology. *MRS Bull.* **24,** 42 (1999).
2. Y. Kawamura, S. Kagao, and Y. Ohno: Electron beam welding of Zr-based bulk metallic glass to crystalline Zr metal. *Mater. Trans.* **42,** 2649 (2001).
3. Y. Kawamura and Y. Ohno: Spark welding of $Zr_{55}Al_{10}Ni_5Cu_{30}$ bulk metallic glasses. *Scripta Mater.* **45,** 127 (2001).
4. Y. Kawamura and Y. Ohno: Metallurgical bonding of bulk metallic glasses. *Mater. Trans., JIM* **42,** 717 (2001).
5. J. Swiston Jr, T.C. Hufnagel, and J.P. Weihs: Joining bulk metallic glass using reactive multilayer foils. *Scripta Mater.* **48,** 1575 (2003).
6. P. Murali and U. Ramamurty: Embrittlement of a bulk metallic glass due to sub-T_g annealing. *Acta Mater.* **53,** 1467 (2005).
7. U. Ramamurty, I.M.L. Lee, J. Basu, and Y. Li: Embrittlement of a bulk metallic glass due to low temperature annealing. *Scripta Mater.* **47,** 107 (2002).
8. N. Nagendra, U. Ramamurty, T.T. Goh, and Y. Li: Effect of crystallinity on the impact toughness of a La-based bulk metallic glass. *Acta Mater.* **48,** 2603 (2000).
9. J. Basu, N. Nagendra, Y. Li, and U. Ramamurty: Microstructure and mechanical properties of partially-crystallized La-based bulk metallic glass. *Philos. Mag.* **83,** 1747 (2003).
10. C.A. Schuh and T.G. Neih: A survey of instrumented indentation studies on metallic glasses. *J. Mater. Res.* **19,** 46 (2004).
11. M.N.M. Patnaik, R. Narasimhan, and U. Ramamurty: Spherical indentation response of metallic glasses. *Acta Mater.* **52,** 3335 (2004).
12. U. Ramamurty, S. Jana, Y. Kawamura, and K. Chattopadhyay: Hardness and plastic deformation in a bulk metallic glass. *Acta Mater.* **53,** 705 (2005).
13. R. Bhowmick, R. Raghavan, K. Chattopadhyay, and U. Ramamurty: Plastic flow softening in a bulk metallic glass. *Acta Mater.* **54,** 4221 (2006).
14. W.C. Oliver and G.M. Pharr: An improved technique for determining hardness and elastic modulus using load and displacement sensing indentation experiments. *J. Mater. Res.* **7,** 1564 (1992).
15. R. Trivedi and W. Kurz: Solidification microstructures: A conceptual approach. *Acta Mater.* **42,** 15 (1994).
16. W. Kurz and D.J. Fusher: Dendrite growth at the limit of stability. Tip radius and spacing. *Acta Metall.* **29,** 11 (1981).
17. G.K. Dey, E.G. Baburaj, and S. Banerjee: Crystallization kinetics of Zr-33at.% Ni amorphous alloy. *J. Mater. Sci.* **21,** 117 (1986).
18. Y.J. Kim, R. Busch, W.L. Johnson, L. Rulison, and W.K. Rhim: Experimental determination of a time-temperature-transformation diagram of the undercooled $Zr_{41.2}Ti_{13.8}Cu_{12.5}Ni_{10.0}Be_{22.5}$ alloy using the containerless electrostatic levitation processing technique. *Appl. Phys. Lett.* **68,** 1057 (1996).
19. W. H. Wang, C. Dong, C. H. Shek: Bulk metallic glasses. *Mater. Sci. Eng., R* **44,** 45 (2004).
20. J.M. Pelletier and B. Van de Moortele: Phase separation and crystallization in the $Zr_{41.2}Ti_{13.8}Cu_{12.5}Ni_{10.0}Be_{22.5}$ bulk metallic glass determined by physical measurements and electron microscopy. *J. Non-Cryst. Solids* **325,** 133 (2003).
21. S. Schneider, P. Thiyagarajan, and W. L. Johnson: Formation of nanocrystals based on decomposition in the $Zr_{41.2}Ti_{13.8}Cu_{12.5}Ni_{10.0}Be_{22.5}$ alloy. *Appl. Phys. Lett* **68,** 493 (1996).
22. X-P. Tang, J.F. Loffler, W.L. Johnson, and Y. Wu: Devitrification of the $Zr_{41.2}Ti_{13.8}Cu_{12.5}Ni_{10.0}Be_{22.5}$ bulk metallic glass studied by XRD, SANS, and NMR. *J. Non-Cryst. Solids* **317,** 118 (2003).